

Chapter 6

Astrometric Precision with MeerKAT

This final Chapter is an expansion (and improvement) on the astrometric routine introduced in Section 3.6.1 (Originally presented in, Hughes et al., 2024). While the properties of SAX J1810 initiated this investigation, as discussed in the following sections, understanding the astrometric evolution of radio core emission Swift J1727 necessitated precise astrometry. Similar to POLKAT, despite the routine being developed to study XRBs, it applies to any point source observations.

6.1 Introduction

Section 2.3.1 introduced several fundamental angular scales, one of which was the angular resolution:

$$\Theta_{\text{PSF}} \sim \frac{\lambda}{d_{\text{max}}}.$$

Quantified by the FWHM (Θ_{PSF}) of the PSF¹, the angular resolution is related to the observing wavelength (λ) and the maximum baseline length (d_{max}). While a reasonable first-order approximation, this equation assumes a circular Gaussian PSF and, thus, rotationally symmetric sampling of the uv -plane. Complex array configurations or non-Zenith observations can cause the projected baseline vectors to be shorter along one dimension, resulting in elliptical Gaussian PSFs. Appropriate uv -weightings can circularize the PSF, even for asymmetric array configurations, at the cost of angular resolution along the more precise direction. Therefore, utilising an interferometer’s full astrometric capabilities necessitates considering PSF ellipticity.

By default, radio synthesis imaging software records the PSF parameters with the FWHM of the major axis (Θ_{maj}), the FWHM of the minor axis (Θ_{min}), and the beam position angle (θ_{bpa}) measured East of North. Given that the PSF is an elliptical Gaussian, the PSF axes can be alternatively expressed as standard deviations, σ_{maj} and σ_{min} , recalling that $\text{FWHM} = \sqrt{8 \ln 2} \sigma$. The PSF is an instrument’s point source response, so the ellipticity manifests as the shape of point sources (e.g., Figure 6.1). To maximize consistency with terminology used at other wavelengths, I adopted the more generic term of a point spread function (PSF) rather than the interferometry-specific terminology of a ‘synthesized beam’. Depending on the resource, what I call a PSF may be referred to as the restoring beam, idealized beam, or synthesized beam; these all correspond to the same concept: the two-dimensional Gaussian fit to the main lobe of the Fourier transform of the uv -sampling function.

The position of a point source is given by the centre of its (PSF-shaped) intensity distribution. Adopting the location of the peak pixel can provide a crude position approximation. However, the peak pixel is affected by pixelization errors if the *actual* peak is situated at a pixel boundary. Pix-

¹Here, I am referencing the idealized PSF, free from finite-sampling effects.

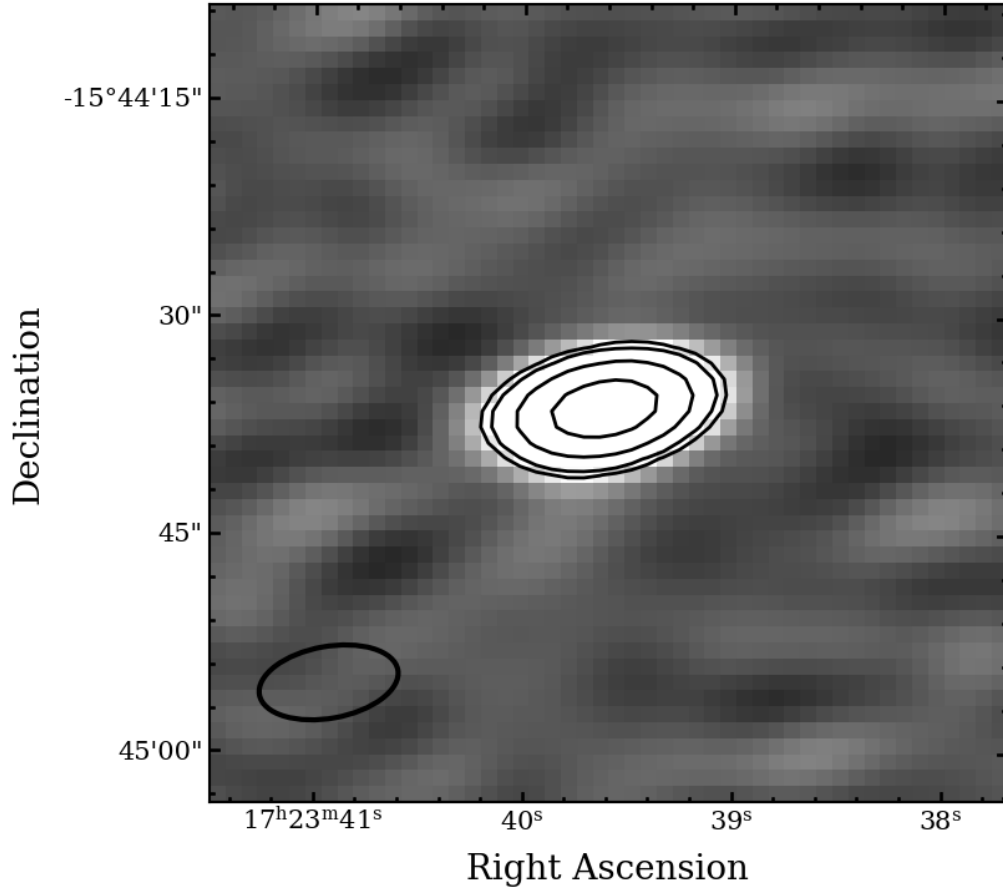


Figure 6.1: Example of a highly elliptical synthesized beam (hollow black ellipse) and its effect on the shape of a point source. In this example, the source was observed at a shallow elevation of $\sim 30^{\circ}$ and an azimuth angle of $\sim 90^{\circ}$. In this example, the relatively low elevation causes relatively high ellipticity, and the azimuth angle rotates the PSF to (roughly) align its major axis with the right ascension axis.

elization errors can be mitigated by decreasing the pixel size, although this approach is prohibitively computationally expensive for interferometers with large fields of view. As a result, the positions of point sources are typically measured by fitting Gaussian components to their intensity distributions, the approach adopted in the previous chapters. Assuming that the pixel size adequately samples the PSF (i.e., $\Theta_{\min} \sim 3\text{--}5$ pixels), Gaussian fitting also mitigates pixelization effects.

Kaper et al. (1966) derived analytic equations for the key parameters and their errors (peak amplitude, central position, and width) measured from one-dimensional Gaussian fitting, assuming uncorrelated Gaussian noise in each pixel. Later, Condon (1997, CR97) derived analytic solutions for two-dimensional data with uncorrelated noise and semi-analytic equations for spatially correlated noise (see also, Condon et al., 1998); the latter applies to synthesis imaging as the PSF acts as a smoothing kernel correlating adjacent pixels. CR97 showed that the variance in the position,

$$\sigma_k^2 = \left(\frac{\mathcal{D}_k}{S/N} \right)^2, \quad (6.1)$$

is a function of the signal-to-noise ratio (S/N) and the *extent* of the Gaussian (\mathcal{D}_k) along direction k (where k is RA or Dec). The extent is a function of the PSF shape, $\mathcal{D}_k = \mathcal{D}_k(\Theta_{\text{maj}}, \Theta_{\text{min}}, \theta_{\text{pa}})$, where elliptical PSFs have $\mathcal{D}_{\text{RA}} \neq \mathcal{D}_{\text{Dec}}$ (see Equations 21 and 41 in CR97). For a circular PSF ($\Theta_{\text{maj}} \equiv \Theta_{\text{min}}$), Equation (6.1) simplifies to,

$$\sigma_k = \frac{\Theta_{\text{maj}}}{\sqrt{8 \ln 2} (S/N)} = \frac{\sigma_{\text{maj}}}{S/N}. \quad (6.2)$$

Some source-finding software packages, like PYBDSF, adopt the CR97 equations to quantify astrometric errors. However, in CR97, the variance was assumed to originate from Gaussian noise, ignoring the effects of sparse uv -sampling or incomplete deconvolution of extended sources, where artefacts

produce large-scale non-Gaussian “noise”. Moreover, Equations (6.1) and (6.2) neglect the potential for signal-to-noise independent systematics from, for example, calibration errors. As a result, many radio astronomers adopt a heuristic astrometric error of the form

$$\sigma_k = \mathcal{D}_k \sqrt{\left(\frac{A}{S/N}\right)^2 + B^2}. \quad (6.3)$$

Consistent with CR97, Equation (6.3) is proportional to the PSF size, scaling inversely with the fitted component’s signal-to-noise ratio, while now including a systematic *floor* on the astrometric error. The next question is obvious: what are the correct choices for \mathcal{D}_k , A , and B ?

Recommendations for A and \mathcal{D}_k can vary depending on who is asked and often are provided without clear justification². For \mathcal{D}_k , a common, conservative assumption is $\mathcal{D}_{\text{RA}} \equiv \mathcal{D}_{\text{Dec}} \equiv \Theta_{\text{maj}}$. Alternatively, the ellipticity is typically accounted for by using the size of the rectangle bounding the PSF,

$$\mathcal{D}_{\text{RA}} = \sqrt{(\Theta_{\text{maj}} \sin \theta_{\text{bpa}})^2 + (\Theta_{\text{min}} \cos \theta_{\text{bpa}})^2}, \quad (6.4)$$

$$\mathcal{D}_{\text{Dec}} = \sqrt{(\Theta_{\text{maj}} \cos \theta_{\text{bpa}})^2 + (\Theta_{\text{min}} \sin \theta_{\text{bpa}})^2}, \quad (6.5)$$

or the lengths from the centre to the ‘edge’ of the PSF,

$$\mathcal{D}_{\text{RA}} = \frac{\sigma_{\text{maj}} \sigma_{\text{min}}}{\sqrt{(\sigma_{\text{maj}} \sin \theta_{\text{bpa}})^2 + (\sigma_{\text{min}} \cos \theta_{\text{bpa}})^2}}, \quad (6.6)$$

$$\mathcal{D}_{\text{Dec}} = \frac{\sigma_{\text{maj}} \sigma_{\text{min}}}{\sqrt{(\sigma_{\text{maj}} \cos \theta_{\text{bpa}})^2 + (\sigma_{\text{min}} \sin \theta_{\text{bpa}})^2}}. \quad (6.7)$$

For A , the most common values adopted in the literature are $A = 1$ and $A = 1/2$, where the latter likely originates from the fact that

²Moreover, many astronomers do not add the A and B components in quadrature, instead adopting the larger of the two.

$1/\sqrt{8\log 2} \approx 1/2.355 \sim 1/2$. To remain approximately consistent with CR97, $A = 1$ **should** be chosen if using *radial* \mathcal{D}_k values (e.g., Equation 6.6 & 6.7) and $A = 1/2$ if using *diameter-like* \mathcal{D}_k values (e.g., Equation 6.4 & 6.5). Incorrect pairings can overestimate errors, potentially leading to missed results, or underestimate errors, artificially increasing the significance of any astrometry-driven phenomenon.

The systematic limit, B , does not have the same theoretical motivation as A and thus can vary significantly from instrument to instrument. The VLA, possibly the best-known interferometer, recommends a systematic error of $\sim 10\%$ the PSF FWHM³. Newer facilities, like MeerKAT, do not have similar recommendations, leading a widespread *ad hoc* adoption of the $\sim 10\%$ VLA systematic. Investigating what systematic limit is appropriate for MeerKAT was the initial motivation for this research.

A last, often overlooked effect is the correlated RA and Dec errors that result from PSFs with principle axes misaligned to these primary directions (i.e., $\theta_{\text{pa}} \neq 0, \pi/2, \pi \dots$). Consider an elliptical PSF with $\theta_{\text{pa}} = \pi/4$; a same-sign deviation (e.g., towards North-East) in RA and Dec is more likely than an opposite-sign deviation (e.g., towards North-West) of equal magnitude. Framing this effect probabilistically, when sampling from a two-dimensional Gaussian, for a fixed radial separation ($r = \sqrt{x^2 + y^2}$), stochastic deviations along the beam position angle are the most likely to occur. While CR97 appropriately treated the co-variances, the heuristic forms of \mathcal{D}_k given by Equations (6.4), (6.5), (6.6), & (6.7) will not enclose the same confidence region for all elliptical PSFs.

This chapter defines a simple yet powerful method to measure astrometric error. Wide-field interferometers like MeerKAT detect thousands of background or foreground point sources in a single observation. The variations in the positions observed during time-domain monitoring of a

³<https://science.nrao.edu/facilities/vla/docs/manuals/oss/performance/positional-accuracy>

single pointing (i.e., *field*) will sample from the underlying astrometric error distribution, allowing for its empirical determination. Ideally, with a large enough sample of targets and pointing, we should better understand the astrometric precision without needing time-domain monitoring of each source.

6.2 Methods

Section 3.6.1 presented an early version of this routine, originally designed to determine the astrometric variability of SAX J1810. Here, I assume the astrometric error adopts a similar functional form as the published version,

$$\hat{\sigma}_r = \sqrt{\left(\frac{A}{S/N}\right)^2 + B^2}. \quad (6.8)$$

The fundamental assumption (based on CR97) is that the astrometric error is proportional to some angular scale $\mathcal{D}_r(\Theta_{\text{maj}}, \Theta_{\text{min}}, \theta_{\text{pa}})$. To account for variable PSFs, I solve for a dimensionless ‘relative astrometric error’ $\hat{\sigma}_r = \sigma_r/\mathcal{D}_r$; where $\hat{\sigma}_r$ is the astrometric error measured in units of ‘PSFs’, and can be converted to physical units given that \mathcal{D}_r is always known. In contrast with the published version, I have refined the method to account for correlated errors by solving for total angular offsets rather than decomposing the offsets into RA and Dec components (hence the change from index \mathcal{D}_k to \mathcal{D}_r).

6.2.1 Offset Geometry

A schematic of the offset geometry is shown in Fig. 6.2. For a single measurement of a point source, stochastic variability offsets the measured position (α, δ) from its true position (α_0, δ_0) by some angular distance r and an offset direction defined by the *offset position angle* (ϕ_{pa}) measured East

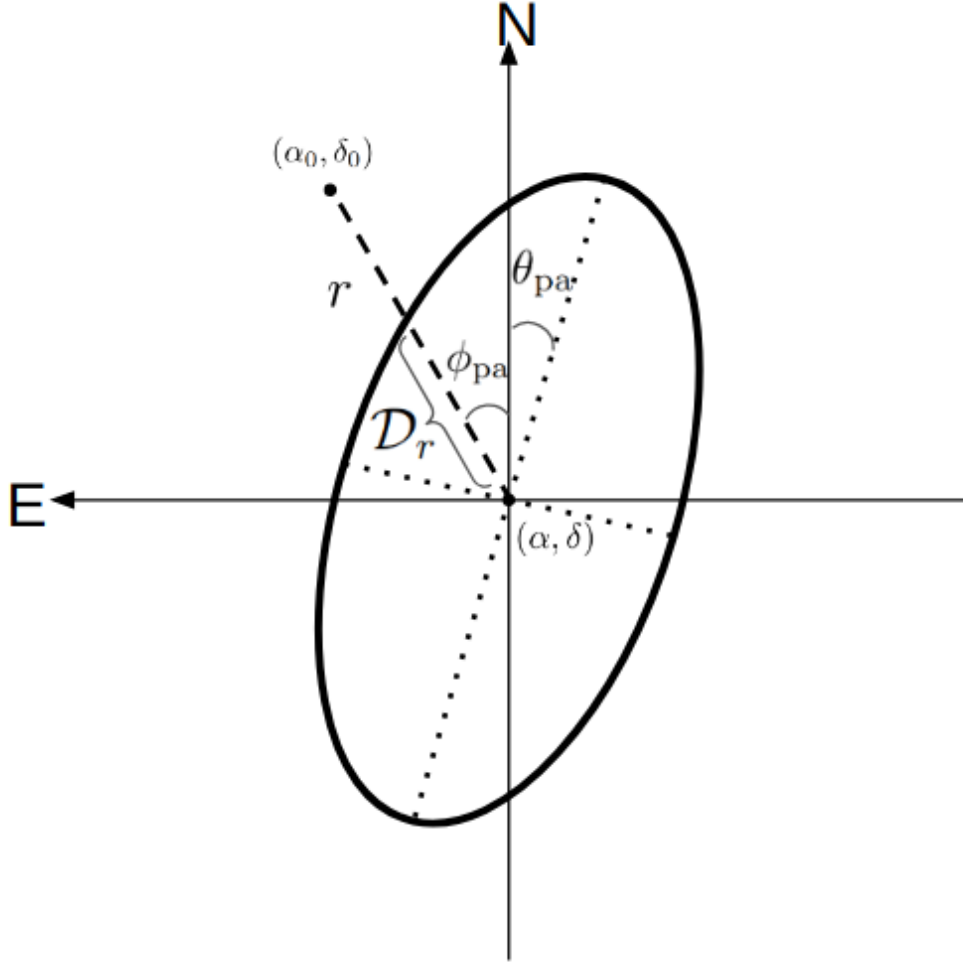


Figure 6.2: Schematic representation of the offset geometry. The measured position, (α, δ) , is offset from the true position, (α_0, δ_0) , by an angular separation \hat{r} . The r is rotated East of North by the offset position angle ϕ_{pa} . \mathcal{D}_r is the distance from (α, δ) to the elliptical confidence region defined by the PSF. The position angle of the elliptical confidence is given by θ_{pa} , but the major and minor axis (represented by the dotted lines) are dependent on the confidence interval of interest (e.g., 68%, 95%, 99.7%, ...)

of North. Similar to the dimensionless astrometric error, the dimensionless separation, $\hat{r} = r/\mathcal{D}_r$, is normalized by the distance from (α, δ) to the elliptical confidence region described by the PSF-shape (shown as a black ellipse in Fig. 6.2)

For an elliptical Gaussian with variances of σ_{maj}^2 and σ_{min}^2 , and no covariance, an arbitrary confidence region is described by,

$$s = \left(\frac{\Delta_{\text{maj}}}{\sigma_{\text{maj}}} \right)^2 + \left(\frac{\Delta_{\text{min}}}{\sigma_{\text{min}}} \right)^2. \quad (6.9)$$

here, Δ_{maj} and Δ_{min} are the zero-point offsets along the major and minor axes, and s depends on the confidence region of interest. Equation (6.9) is the sum of the squares of independent normally distributed variables, and thus s follows the χ_ν^2 -distribution for two degrees of freedom ($\nu = 2$),

$$P(\chi_{\nu=2}^2 \leq s) = P_0, \quad (6.10)$$

for a confidence region probability, P_0 . We choose $P_0 = 0.68$ (1σ), and thus $s \approx 2.279$ given a χ_ν^2 -distribution with two degrees of freedom. However, the choice is arbitrary, and different P_0 values will scale A and B appropriately, as long as P_0 remains consistent for observations with different PSF shapes. The confidence region is an ellipse with major and minor axes equal to $\sqrt{s} \sigma_{\text{maj}}$ and $\sqrt{s} \sigma_{\text{min}}$, respectively. Recognizing that the line connecting (α_0, δ_0) and (α, δ) passes through the ellipse at an angle of $\xi = \phi_{\text{pa}} - \theta_{\text{pa}}$,

$$\Delta_{\text{min}} = \Delta_{\text{maj}} \tan \xi, \quad (6.11)$$

where Δ_{maj} and Δ_{min} are the offset angles along the major and minor axis, respectively. Thus, Equation (6.9) becomes:

$$\Delta_{\text{maj}} = \frac{\sqrt{s} \sigma_{\text{maj}} \sigma_{\text{min}}}{\sqrt{\sigma_{\text{min}}^2 + (\sigma_{\text{maj}} \tan \xi)^2}}, \quad (6.12)$$

and \mathcal{D}_r is defined as,

$$\mathcal{D}_r = \sqrt{\Delta_{\text{maj}}^2 + \Delta_{\text{min}}^2}. \quad (6.13)$$

Knowledge of the measured position, true position, and PSF properties is sufficient to solve for r , \mathcal{D}_r , and thus, \hat{r} . As \hat{r} is positive definite, repeated observations of an arbitrary source j will sample a Rayleigh distribution with a scale factor equivalent to the dimensionless astrometric error, $(\hat{\sigma}_r)_j$. For a source observed over N epochs, we can estimate its astrometric error from the sample distribution (Siddiqui, 1964),

$$(\hat{\sigma}_r)_j \approx \frac{\Gamma(N)\sqrt{N}}{\Gamma(N + \frac{1}{2})} \sqrt{\frac{1}{2N} \sum_{i=1}^N \hat{r}_{i,j}^2}. \quad (6.14)$$

Monitoring several sources at different signal-to-noise ratios is sufficient to derive A and B from Equation (6.8).

6.2.2 Workflow

I developed the following routine that uses the positional variability of field sources to determine an astrometric error in time-domain observations. Assuming a single image has been made for each observation, we use PYBDSF to make per-observation source catalogues. PYBDSF models the sky intensity distribution as a collection of Gaussian *components*. Components are then grouped into *sources* based on their relative separations and intensities⁴. The sources are then associated with *islands* — contiguous regions of pixels with values greater than some threshold value (`thresh_isl` in PYBDSF), and at least one pixel greater than the source detection threshold (`thresh_pix` in PYBDSF); both thresholds are expressed in units of rms devi-

⁴see <https://pybdsf.readthedocs.io/en/latest/algorithms.html> for more information

ations from the mean background intensity. I chose values of `thresh_isl=3` and `thresh_pix=4`.

The PYBDSF source catalogues include the peak intensity (F_p), the island flux density (F_i), and the source sizes quantified by major (Θ_M) and minor (Θ_m) axes. PYBDSF also classified each source as S- (single-component source, single-source island), C- (single-component source, multi-source island), or M-type (multi-component source).

I am interested in the astrometric error for the point source fitting. Thus, I remove resolved sources from the catalogues. To make it easier to identify point sources, the shapes of all Gaussian components are fixed to that of the PSF (`fix_to_beam=True` in PYBDSF), and components within an island are grouped into a single source (`group_by_isl=True` in PYBDSF). These flags make the classification binary, with S-types and (C or M)-types corresponding to point sources and resolved sources, respectively. By definition, all S-type sources will follow the strict definition of a point source; $F_i \sim F_p$ ⁵, $\Theta_M \equiv \Theta_{\text{maj}}$, and $\Theta_m \equiv \Theta_{\text{min}}$. However, noise fluctuations or imaging artefacts can cause PYBDSF to fit additional sub-dominant components, causing some point sources to be misclassified as resolved. To avoid removing an excessive number of sources, I adopt an empirically motivated “point-like” definition,

$$\begin{aligned} \frac{F_i}{F_p} - 1 &< \delta_F, \\ \left| \frac{\Theta_M}{\Theta_{\text{maj}}} - 1 \right| &< \delta_S, \text{ and} \\ \left| \frac{\Theta_m}{\Theta_{\text{min}}} - 1 \right| &< \delta_S, \end{aligned}$$

allowing small tolerances, δ_F and δ_S . I chose to set $\delta_F = \delta_S = 0.1$ (i.e., PYBDSF measures the source to be within 10% of an ideal point source).

⁵The reason why the flux condition is left as an approximation is due to the definition of an Island. Pixel variations in each island can result in negligible (but finite) differences between the integrated island flux density and peak intensity

I apply an off-axis cutoff, excluding sources $> 0.3^\circ$ from the phase centre, corresponding to a (normalized) primary beam power of $\mathcal{A} > 75\%$. This exclusion of these off-axis sources minimizes the errors from direction-dependent effects, which can affect the quality of both phase (i.e., position) and amplitude calibration (see, e.g., Smirnov, 2011a,b, and references therein). Lastly, I exclude highly variable and transient sources that would exhibit significant changes in their signal-to-noise ratios. Any sources with maximum and minimum peak intensities separated by a factor ≥ 2 or missing from $\geq 25\%$ of the epochs are removed from each catalogue. The astrometry routine proceeds as follows:

- Step 1: With PYBDSF, extract a catalogue of each observation, removing sources that fail the point-like conditions. The catalogues are cross-matched to one another, adopting a single observation as the reference. Sources separated by less than $\Theta_{\text{maj}}/3$ are taken as matches. The final catalog consists of n_{obs} observations of n_{src} sources, such that each source j has a position $(\alpha_{i,j}, \delta_{i,j})$ and a signal-to-noise of $(S/N)_{i,j}$, in observation i .
- Step 2: Calculate the average position of each source (average over index j), weighting each observation with the size of the PSF along the RA and Dec directions (to the 68% confidence region); i.e., inverse-variance weightings, $\mathcal{D}_{\text{RA}}^{-2}$ and $\mathcal{D}_{\text{Dec}}^{-2}$, respectively.
- Step 3: Bootstrap the positions to estimate the uncertainty on $(\hat{\sigma}_r)_j$. For each source, create n_{boot} bootstrapped samples of length n_{obs} , re-sampling (with replacement) the positions from each observation. Assuming the average value from (2) represents the true position of each source, calculate the dimensionless astrometric errors in each bootstrap sample. I used $n_{\text{boot}} = 1000$.

- Step 4: For each source, adopt the median value from the bootstrapped samples as $(\hat{\sigma}_r)_j$, quantifying the 1σ confidence interval as half the range between the 16th and 84th percentile. The routine outputs the ratio of positive (median to 84th percentile) and negative (16th to median) errors to investigate whether the errors are asymmetric; asymmetric errors (i.e., if the ratio is not close to unity) will invalidate the likelihood function as it assumes normally distributed variables.
- Step 5: Calculate the median signal-to-noise ratio for each source, $(S/N)_j$.
- Step 6: Solve for the astrometric error parameters A and B . We solve for A and B with a similar MCMC approach as applied in Section 3.2.3. Assume $(\hat{\sigma}_r)_j$ values are independent and normally distributed, adopting flat uninformative priors for A and B , with the only constraint being that $A \geq 0$ and $B \geq 0$ (we chose an arbitrary, large upper bound). These A and B values quantify the *uncorrected* astrometric error.
- Step 7: Solve for the per-observation average astrometric correction (average across index i) in RA and Dec. The averages are inverse-variance weighted, using the parameters from Step 6 and Equation 6.8.
- Step 8: Correct the positions with the per-observation corrections and repeat Steps 1–7 until the corrections converge (see Step 9). The uncertainty on the per-observation correction is included in each subsequent bootstrap subsample. This is done by adding a random offset drawn from a normal distribution with a standard deviation fixed to the uncertainty in the per-observation correction.

Step 9: I define the convergence parameter C between run n and $n + 1$ as:

$$C = \frac{|(\hat{\sigma}_{r,j})_{n+1} - (\hat{\sigma}_{r,j})_n|}{\sqrt{(\Delta\hat{\sigma}_{r,j})_{n+1}^2 + (\Delta\hat{\sigma}_{r,j})_n^2}}.$$

I consider convergence to have occurred after $C < 0.1$ for three consecutive iterations. The final values of A and B quantify the *corrected* astrometric error.

I made this routine (ASTKAT) publicly available⁶. It also allows the user to simulate images for code verification, as well as modify the parameters that control cataloguing, filtering, bootstrapping, and convergence. I solve for \mathcal{D}_{RA} and \mathcal{D}_{Dec} by marginalizing the PSF along the RA and Dec directions, respectively. I then use these values to estimate errors on individual RA and Dec measurements.

6.3 Results

The astrometric fit for the three XRB fields discussed in this thesis are presented in Figures 6.3–6.5. Additionally, I tabulate the fit parameters in Table 6.1, including the reduced statistic χ_{red}^2 and a ‘fractional FWHM equivalent’ ($B \times \sqrt{s/8 \ln 2}$) to quantify the systematic astrometric limit as a fraction of the PSF FWHM.

⁶<https://github.com/AKHughes1994/AstKAT>